Retrograde equatorial surface flows generated by thermal convection confined under a stably stratified layer in a rapidly rotating spherical shell

Shin-ichi Takehiro†* , Michio Yamada†, and Yoshi-Yuki Hayashi‡

†Research Institute for Mathematical Sciences, Kyoto University, Kyoto 606-8502, Japan

‡Department of Earth and Planetary Sciences, Kobe University, Kobe 657-8501, Japan

Finite amplitude thermal convection in a rapidly rotating spherical shell associated with a stably stratified layer placed near the outer surface is investigated. Systematic numerical experiments are performed with an Ekman number of $E = 10^{-3}$, a Prandtl number of $P = 1$ and an inner/outer radius ratio of $\eta = 0.4$, and the existence of a strongly stratified upper layer is shown to enhance the generation of equatorial surface retrograde flows when the Rayleigh number is approximately ten times larger than the critical value. The existence of the stable layer causes the bottom of the stable layer to behave as a virtual boundary for the convective motion underneath. Its effective dynamic condition varies from the free-slip condition to the no-slip condition as the Rayleigh number increases. The Reynolds stress of the convective vortices beneath the stable layer is weakened and is dominated by the transport of the planetary angular momentum. As a result, the latitudinal temperature gradient produced at the bottom of the stable layer induces the equatorial retrograde flow through the thermal wind balance. This diffuses through the stable layer by viscosity and produces the equatorial surface retrograde flow.

Keywords: mean zonal flows, stably stratified layer, angular momentum budget, viscous diffusion

1   INTRODUCTION

The banded structure of the zonal flows observed in the giant planets is one of the most prominent phenomena of planetary atmospheric motions. Among the characteristics of the banded structure, the directions of the equatorial zonal flows are remarkable. Uranus and Neptune have equatorial retrograde flows (Hammel *et al.* 2005, Sromovsky *et al.* 2001), whereas Jupiter and Saturn have prograde, that is, equatorial superrotation flows (Garcia-Melendo and Sanchez-Lavega 2001, Sanchez-Lavega *et al.* 2000). An equatorial prograde flow is also observed in the sun (Thompson *et al.* 1996). The equatorial superrotation state is interesting from a dynamics point of view. Since the equatorial upper layer is the farthest region from the planetary rotating axis, a simple axisymmetric mixing induces a retrograde zonal flow because of the conservation of angular momentum. A particular mechanism must operate to generate and maintain the equatorial superrotation state.

In order to explain the acceleration mechanism at the top of the equator, possible roles of thermal convection in rotating spherical shells have been investigated. Since the observations of thermal emission show that, with the exception of Uranus, the giant planets have heat sources in the interiors (Pearl and Conrath 1991), convective motions have been considered to exist in the deep layers below the cloud layers. The first derivation of a solution of equatorial surface prograde flows was performed by Busse (1970) for the case of a slowly rotating spherical shell. In the rapidly rotating cases, weakly non-linear and finite amplitude calculations have demonstrated that the mean zonal flows induced by convection tend to be prograde at the top of the equator when the Prandtl number is on the order of unity or less (Zhang 1992, Takehiro and Hayashi 1999, Aurnou and Olson 2001, Christensen 2002). Taylor-column type vortices along the axis of rotation are tilted in the prograde outward direction due to the heterogeneity of the topographic β effect of the outer boundary (Takehiro 2008). Reynolds stress caused by the tilting transports angular

---

*Corresponding author. Email: takepiro@gfd-dennou.org

momentum from the inner to outer regions. As a result, the equatorial superrotation state emerges [1]. This mechanism becomes ineffective when the Rayleigh number is increased to a degree that the buoyancy force dominates the Coriolis force, and a retrograde flow is induced at the top of the equator due to homogenization of angular momentum (Gilman 1977, Aurnou *et al.* 2007).

Most of the studies on thermal convection in rotating spherical shells consider situations in which the entire layer is thermally unstable. However, the actual planetary atmospheres may not consist of entirely unstable layers (e.g. Guillot 1999, 2005). There exist stable stratospheres (Hunt 1983) and possibly moderately stable cloud layers (Sugiyama *et al.* 2006). Below the cloud layer, the Galileo spacecraft observed a stable layer between depths of 5 and 16 bars in the Jovian atmosphere (Seiff *et al.* 1996). If such a stable layer exists near the top boundary, then the generation of mean zonal flow caused by the angular momentum transport due to the tilting convection cells might not operate because the convective motion could not penetrate the stable layer depending on the strength of stratification.

There are a few studies of thermal convection in rotating spherical shells with upper stably stratified layers. Zhang and Schubert (1996, 1997) obtained the critical convection and illustrated the perfect penetration of the Taylor-column type convection into the stable layer. On the other hand, Takehiro and Lister (2001) theoretically derived a penetration distance of columnar convection from the dispersion relation of inertial gravity waves. The distance is shown to be proportional to the ratio between the angular velocity of the shell Ω and the Brunt-Väisälä frequency of the stable layer N. They clarified that that the solutions of Zhang and Schubert correspond to large Ω/N cases. Numerical time integrations of finite amplitude convection are performed by Takehiro and Lister (2002) for cases of Rayleigh numbers that are several times larger than the critical value. They showed that the penetration extent of convective motion is actually determined by Ω/N. However, equatorial prograde mean zonal flows induced at the bottom of the stable layer diffuse to the surface, even when convective motion is trapped below the stratified layer.

Recently, MHD dynamo calculations in a rapidly rotating spherical shell with an outer stably stratified layer have also been performed. Flows in the overlying stable layer have been reported to be important to the magnetic field in the outer region (Schubert *et al.* 2004). The directions of resultant equatorial zonal flows are diverse: a retrograde zonal flow at the top of the equator was obtained by Christensen (2006), whereas prograde zonal flows were obtained by the calculations of Stanley and Mohammadi (2008) and Christensen and Wicht (2008).

In the present study, we perform systematic numerical experiments of finite amplitude thermal convection in a rotating spherical shell with an upper stably stratified layer. We focus on the mechanism of surface zonal flow generation and the role of the upper stable layer rather than direct applications to the actual planetary atmospheres. For this reason, we use the Boussinesq approximation, which is also used in the studies mentioned above. The set up is modified from that of Takehiro and Lister (2002) in the following manner. The thickness of the stratified layer is reduced to enlarge the convective region. The value of the Rayleigh number is extended to approximately several dozen times larger than the critical value, while the value of the Ekman number is increased to ten times that used in Takehiro and Lister (2002) in order to systematically perform several calculations. We investigate the change in the mean zonal flow generated by thermal convection as the stratification strength of the stable layer and the Rayleigh number are varied.

2   MODEL

Let us consider a Boussinesq fluid filling a shell with inner and outer radii r_i^* and r_o^*, respectively. The shell rotates with angular velocity Ω. The super-adiabatic temperature gradient of the basic state is given

---

[1]Glatzmaier *et al.* (2008) recently proposed that turbulent convection of non-Boussinesq fluid does not constitute geostrophic convection columns but can still produce and maintain equatorial prograde flows by local generation of vorticity through expansion/contraction of rising/sinking plumes. In the present study, we concentrate on the convection of Boussinesq fluid. An extension to non-Boussinesq cases is left for future studies.

in the following form (Takehiro and Lister 2001, 2002):

$$\frac{dT_B^*}{dr^*} = -\frac{1}{2}\left(\frac{Q_0 r^*}{3k} + \Gamma_0^*\right)\left[1 - \tanh\frac{r^* - r_b^*}{a^*}\right] + \Gamma_0^*, \tag{1}$$

where r^* is the radius from the center of the spherical shell, $T_B^*(r^*)$ is the temperature of the basic state, r_b^* indicates the boundary between the lower unstable region and the upper stable region, a^* denotes the thickness of the transition layer, and k is the thermal conductivity. The temperature gradient in the inner region is determined by the uniform internal heat source Q_0, and the outer region is determined by the constant temperature gradient Γ_0^*. The temperature profile is connected continuously around $r^* = r_b^*$. That is,

$$\frac{dT_B^*}{dr^*} \approx \begin{cases} -Q_0 r^*/3k & (r^* \ll r_b^* - a^*), \\ \Gamma_0^* & (r^* \gg r_b^* + a^*). \end{cases} \tag{2}$$

We choose the thickness of the shell $D = r_o^* - r_i^*$ as the length scale, the viscous diffusion time D^2/ν as the time scale, and the viscous velocity ν/D as the velocity scale, where ν is the kinematic viscosity. The temperature is scaled by the internal heat source as $Q_0 D^2/(3k)$, and non-hydrostatic pressure p is scaled by $\rho\nu\Omega$. The governing equations are

$$E\left(\frac{\partial \mathbf{u}}{\partial t} + \mathbf{u}\cdot\nabla\mathbf{u} - \nabla^2\mathbf{u}\right) + 2\mathbf{k}\times\mathbf{u} + \nabla p = R\frac{\mathbf{r}}{r_o}T, \tag{3}$$

$$\frac{\partial T}{\partial t} + \mathbf{u}\cdot\nabla T + u_r\frac{dT_B}{dr} = \frac{1}{P}\nabla^2 T, \tag{4}$$

$$\nabla\cdot\mathbf{u} = 0, \tag{5}$$

where $\mathbf{u}$ is velocity and T is the temperature disturbance. The non-dimensional parameters,

$$R = \frac{\alpha g_o Q_0 D^3}{3k\nu\Omega}, \quad E = \frac{\nu}{\Omega D^2}, \quad P = \frac{\nu}{\kappa}, \tag{6}$$

in the governing equations are the modified Rayleigh number, the Ekman number, and the Prandtl number, respectively. Here, α is the thermal expansion coefficient, g_o is the gravity at the outer boundary of the shell, and κ is the thermal diffusivity. In addition, u_r is the radial component of the velocity.

The conditions at the boundaries are free-slip and fixed temperature:

$$\mathbf{r}\cdot\mathbf{u} = 0, \quad \frac{\partial}{\partial r}\left(\frac{\mathbf{u}\times\mathbf{r}}{r^2}\right) = \mathbf{0}, \quad T = 0, \quad \text{at} \quad r = \frac{\eta}{1-\eta} \quad \text{and} \quad \frac{1}{1-\eta}, \tag{7}$$

where $\eta = r_i/r_o$ is the ratio between the inner and outer radii of the shell, and $r_i = r_i^*/D = \eta/(1-\eta)$ and $r_o = r_o^*/D = 1/(1-\eta)$ are the non-dimensional boundary radii. The non-dimensional basic temperature is given by

$$\frac{dT_B}{dr} = -\frac{1}{2}(r + \Gamma_0)\left[1 - \tanh\frac{r - r_b}{a}\right] + \Gamma_0. \tag{8}$$

Here, $\Gamma_0 = \Gamma_0^* \cdot 3\kappa/(Q_0 D)$, $r_b = r_b^*/D$, and $a = a^*/D$ are the non-dimensional temperature gradient in the outer layer, and the radial position and thickness of the transition layer, respectively. Figure 1 shows typical profiles of temperature, the temperature gradient of the basic state, and the internal heat source.

The important parameter for the extent of penetration Ω/N in the stable layer is described by these
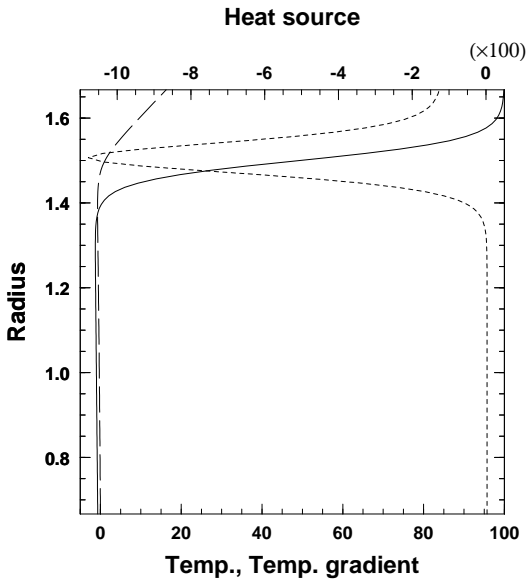
Figure 1.   The profiles of temperature, the temperature gradient, and the internal heat source of the basic state for the case of $\Gamma_0 = 10$. Broken, solid, short-dashed lines denote temperature, the temperature gradient, and the heat source, respectively. The geometry parameters are fixed as $\eta = 0.4, r_b = 1.5$, and $a = 0.05$ for all of the cases.

non-dimensional parameters as follows:

$$\frac{\Omega}{N} = \frac{\Omega}{\sqrt{\alpha g_o \Gamma_0^*}} = \sqrt{\frac{3k\nu\Omega}{\alpha g_o Q_0 D^3}} \frac{\Omega D^2}{\nu} \frac{Q_0 D}{3k} \frac{1}{\Gamma_0^*} = \frac{1}{\sqrt{RE\Gamma_0}}. \tag{9}$$

The calculations of critical convection reveal that Taylor-column type convection deeply penetrates the stable layer when $(\Omega/N)k_H$ is larger than the thickness of the stable layer, whereas the penetration is weakened when $(\Omega/N)k_H$ is less than the thickness of the stable layer (Takehiro and Lister 2001). Here, k_H is a typical horizontal wavenumber of the convective motion. This scaling law is confirmed to be applicable to the finite amplitude convection at a Rayleigh number several times greater than the critical value (Takehiro and Lister 2002).

In the following, we will perform numerical time integrations using larger values of the Rayleigh number than those used in Takehiro and Lister (2002). The Rayleigh number is varied from a few times to approximately forty times the critical value R_c. The temperature gradient in the stable layer Γ_0 is also extended and is varied from 1 to 10^4. The radius ratio and the Prandtl number are fixed as $\eta = 0.4$ ($r_i = 0.667, r_o = 1.667$), and $P = 1$, respectively. The Ekman number is $E = 10^{-3}$, which is increased to ten times that used in Takehiro and Lister (2002) in order to perform several systematic experiments. The parameters for the stable layer are given as $r_b = 1.5$ and $a = 0.05$, where the thickness of the layer is reduced from Takehiro and Lister (2002) to enlarge the convective region. The important parameters Ω/N and the supercriticality R/R_c for each experiment are summarized in Table 1. The initial condition is given as the state of rest $\mathbf{u} = \mathbf{0}$ accompanied by a point-like temperature disturbance with an amplitude of 0.01. The actual time integrations are performed using the equations described by the toroidal and poloidal potentials. The equations are expanded by the spherical harmonics in the horizontal direction and by the Chebyshev polynomials in the radial direction. The spherical harmonics are truncated at a total wavenumber of 42 or 85, and Chebyshev polynomials are calculated up to the 32nd or 48th order. In all of the calculations, the kinetic energy becomes almost stationary by one non-dimensional time. The calculated data between 1 and 1.2 non-dimensional time units are subjected to the following analyses. For the spectral transform calculations, the Fortran77 library "ISPACK" (http://www.gfd-dennou.org/library/ispack/) and its Fortran90 wrapper library "SPMODEL library"(Takehiro *et al.* 2006) (http://www.gfd-dennou.org/library/spmodel/) were used.

Γ_0	10^0	10^1	10^2	10^3	10^4
$R = 2.0 \times 10^3$	0.71,44.5	0.22,43.0	0.071,43.0	0.022,23.9	0.0071,19.6
1.5×10^3	0.82,34.1	0.26,32.6	0.08,32.6	0.026,17.9	0.0082,14.7
1.0×10^3	1.0, 22.7	0.32,21.5	0.10,21.5	0.032,11.9	0.010,9.80
5.0×10^2	1.4,11.4	0.45,10.8	0.14,10.8	0.045,6.00	0.014,4.90
2.0×10^2	2.2,4.5	0.71,4.30	0.22,4.30	0.071,2.39	0.022,1.96
1.0×10^2			0.32,2.15	0.10,1.19	

Table 1. Values of Ω/N (left) and R/R_c (right) for each case of the numerical experiments, where R_c is the critical Rayleigh number.
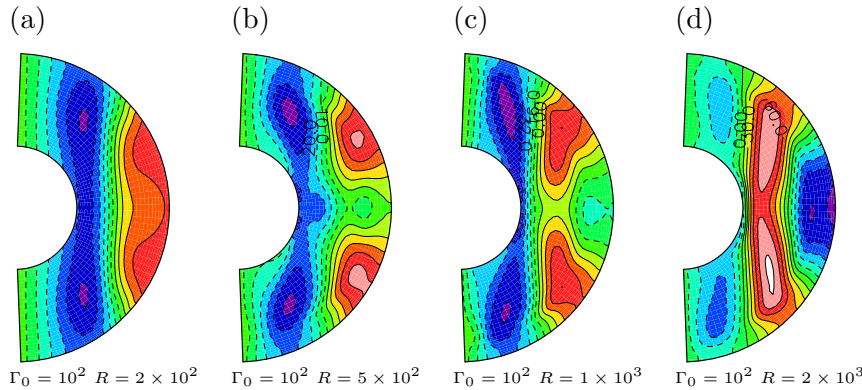

Figure 2. Mean zonal flow distributions for various values of the Rayleigh number with $\Gamma_0 = 100$. Solid lines and red regions indicate prograde flows, and broken lines and blue regions indicate retrograde flows (colour online). The temporal mean fields between 1 and 1.2 non-dimensional time units are shown. The contour interval is 4 in (a), 5 in (b), 8 in (c), and 15 in (d). Note that the critical Rayleigh number is $R_c = 46.5$.

3   RESULTS

Figure 2 shows mean zonal flow distributions for various values of the Rayleigh number when the temperature gradient in the stable layer is fixed. For a Rayleigh number five times greater than the critical value (figure 2(a)), the distribution of mean zonal flow is largely uniform along the axis of rotation and is prograde in the outer equatorial region. This mean zonal flow distribution is similar to that of the weak stratification cases reported by Takehiro and Lister (2002). However, as the Rayleigh number is increased, the retrograde region begins to penetrate the stable layer around the equator and extends to the outer boundary (figure 2(b)), and, finally, retrograde flows are dominant from the equator to the mid-latitudes (figures 2(c) and 2(d)).

Figure 3 shows the variation of the mean zonal flow distributions when the temperature gradient of the upper stable layer is increased while the value of the Rayleigh number is fixed. In the case of weak stratification, $\Gamma_0 = 1$ (figure 3(a)), the distribution is completely uniform along the axis of rotation, and prograde mean flows are induced in the outer region far from the axis of rotation, while retrograde flows are generated in the inner region near the axis. This distribution is close to that for the case without the upper stratified layer. However, as the temperature gradient is increased, the retrograde region breaks through the stratified layer and reaches the outer boundary (figures 3(b) through 3(d)), and the retrograde flows again dominate the equatorial and high-latitude regions (figure 3(e)).

Figure 4 is the diagram of mean zonal flow distributions versus the temperature gradient of the stable layer and the Rayleigh number. In the cases of Rayleigh numbers of several times the critical value, equatorial prograde flows appear in the outer region for all of the temperature gradient values. This is consistent with the results of Takehiro and Lister (2002). However, for larger values of the Rayleigh number, the increase in stratification of the stable layer causes retrograde flows in the equatorial outer region. The retrograde flow tends to emerge when Ω/N is smaller than unity and the value of the Rayleigh number is larger than ten times the critical value. Note that these retrograde flows are not caused by angular momentum homogenization. The amplitudes of the flows shown in figures 2 and 3 are so weak that the magnitudes of their relative angular momentum are much smaller than the planetary angular momentum. On the other hand, when the stratification of the stable layer is weak, i.e., Ω/N is approximately unity,
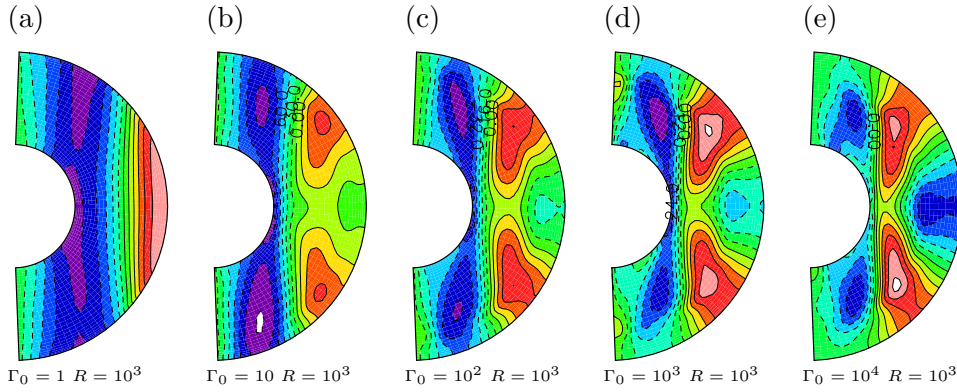
(a)   (b)   (c)   (d)   (e)

$\Gamma_0 = 1 \ R = 10^3$ $\Gamma_0 = 10 \ R = 10^3$ $\Gamma_0 = 10^2 \ R = 10^3$ $\Gamma_0 = 10^3 \ R = 10^3$ $\Gamma_0 = 10^4 \ R = 10^3$

Figure 3. Mean zonal flow distributions for various values of the stable layer temperature gradient Γ_0 with $R = 1 \times 10^3$ (colour online). The contour interval is 30 in (a), 15 in (b), 8 in (c), and 6 in (d) and (e).
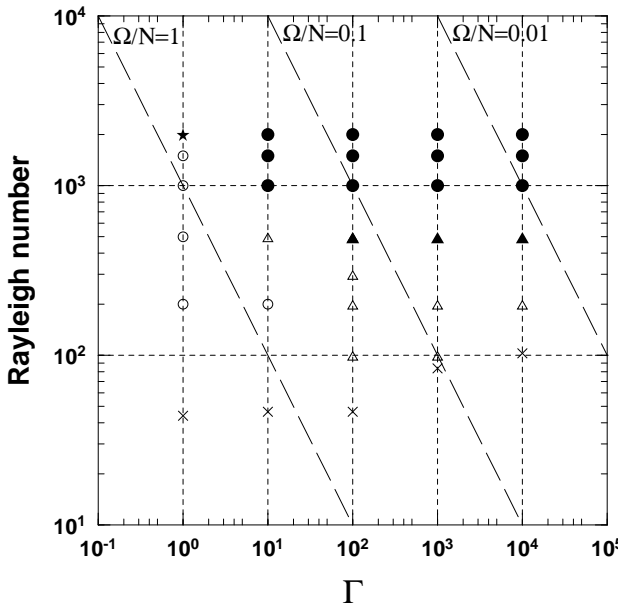

Figure 4. Pattern diagram of the mean zonal flow distributions with respect to the temperature gradient of the stable layer and the Rayleigh number. White and black symbols denote the equatorial prograde and retrograde flows at the outer boundary, respectively. White circles indicate the distributions that are largely uniform along the axis of rotation, as shown in figure 3(a). Crosses denote the critical states. White triangles indicate the distributions that are distorted from the axially uniform fields in the equatorial outer region, as shown in figure 2(a). Black triangles denote the distributions in which the retrograde flows elongate from the equatorial inner to outer regions, as shown in figure 2(b). Black circles indicate the distributions accompanied by the isolated retrograde regions in the equatorial outer stable layer, similar to figure 2(d). The black asterisk indicates the equatorial retrograde flow at the outer boundary produced by angular momentum homogenization.

the Rayleigh number should be increased, for example, up to 2×10^3 for $\Gamma_0 = 1$ in order to obtain the equatorial retrograde surface flow. This equatorial retrograde flow is produced by angular momentum homogenization due to vigorous convective motions (Gilman 1977, Aurnou *et al.* 2007).

In order to illustrate the behavior of the convective motion, figure 5 shows snapshots of the radial component of velocity. In the case of $\Omega/N = 0.22$ and $R/R_c = 4.30$ (figure 5(a)), in which the equatorial mean zonal flow is prograde (figure 2(a)), systematic Taylor-columnar convection emerges outside the tangent cylinder below the stable layer, but does not penetrate the stable layer. When the Rayleigh number is increased to $R/R_c = 21.5$ but the stratification is maintained approximately constant at $\Omega/N = 0.1$ (figure 5(b)), where the equatorial mean zonal flow is retrograde (figures 2(c) and 3(c)), the irregular convective motion breaks the columnar structure, but is still confined under the stable layer. The convective motion also occurs inside the tangent cylinder. When the stratification is weakened to $\Omega/N = 1$ but the Rayleigh number is maintained approximately constant at $R/R_c = 22.7$ (figure 5(c)), where the equatorial
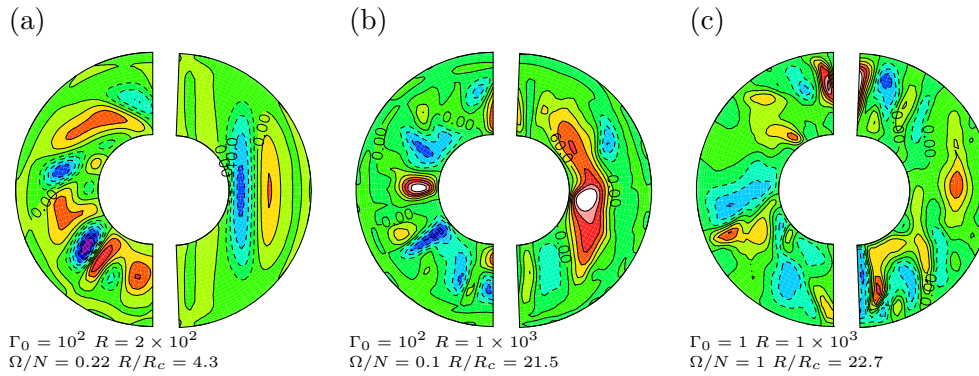
Figure 5. Snapshots of the radial component of the velocity field at 1.2 non-dimensional time units. The left-hand and right-hand panels for each case show the equatorial cross section and a meridional cross section, respectively. Solid lines and red regions indicate radially outward motion, and broken lines and blue regions indicate radially inward motion (colour online). The contour interval is 5 in (a) and 30 in (b) and (c).
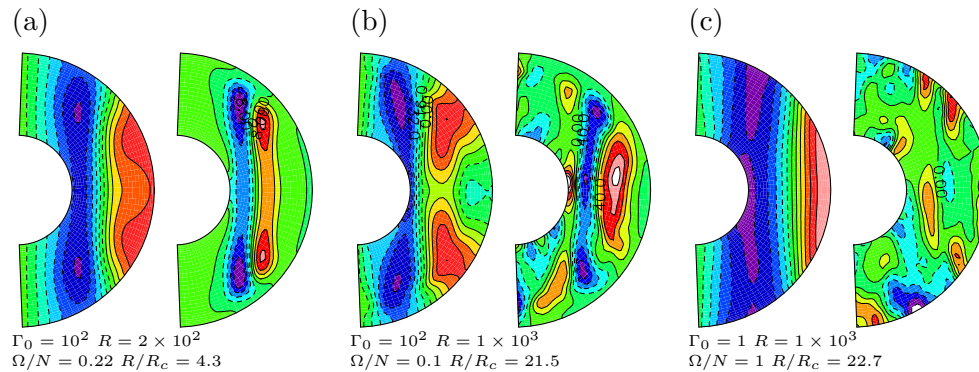

Figure 6. Snapshots of the disturbance component of azimuthal velocity at the same time and the same meridional cross section shown in figure 5 (right), and temporally averaged zonal mean component of azimuthal velocity (left). The left-hand panels are from figures 2(a), 2(c), and 3(a), respectively. Solid lines and red regions indicate the prograde direction, whereas broken lines and blue regions indicate the retrograde direction (colour online). The values of Γ_0 and R are the same as the values shown in figure 5 for each case. The contour intervals are (a) 4 for zonal mean and 4 for disturbance, (b) 8 for zonal mean and 20 for disturbance, and (c) 30 for zonal mean and 40 for disturbance.

mean zonal flow is prograde (figure 3(a)), the convective motion fully penetrates and erodes the stable layer.

The extent of penetration of the convective motions is shown in figure 6, where the longitudinal component of velocity is divided into the zonal mean and the disturbance from the zonal mean. For the case in which $\Omega/N = 0.22$ and $R/R_c = 4.30$ (figure 6(a)), Taylor-column type convective motion is trapped below the stable layer, whereas the mean zonal flow extends into the entire stable layer. When the Rayleigh number is increased to $R/R_c = 21.5$ but the stratification is maintained approximately constant at $\Omega/N = 0.1$ (figure 6(b)), the convective motion becomes irregular but is still confined beneath the stable layer, as indicated by the radial motion of figure 5(b). Once again, the zonal mean component fully extends into the stable layer. However, the zonal flow appears to penetrate in the radial direction rather than in the direction of the axis of rotation. When the stratification is weakened to $\Omega/N = 1$ but the Rayleigh number is maintained approximately constant at $R/R_c = 22.7$ (figure 6(c)), the amplitude of the disturbance is also strong in the stable layer, which indicates that the convective motion completely erodes the stable layer. As a result of the erosion of the stable layer, the distribution of the induced mean zonal flow is similar to that observed in previous studies without a stable layer (Zhang 1992, Takehiro and Hayashi 1999, Aurnou and Olson 2001).

Figure 7 shows the convective motions through the vorticity component in the direction of the rotating axis. The aspect of penetration observed in the previous figures can be confirmed again. For the case in which $\Omega/N = 0.22$ and $R/R_c = 4.30$ (figure 7(a)), regular Taylor-columnar convection columns are trapped below the stable layer. When the Rayleigh number is increased to $R/R_c = 21.5$ but the stratification is maintained approximately constant at $\Omega/N = 0.1$ (figure 7(b)), the irregular convective motion breaks the

(a)   (b)   (c)

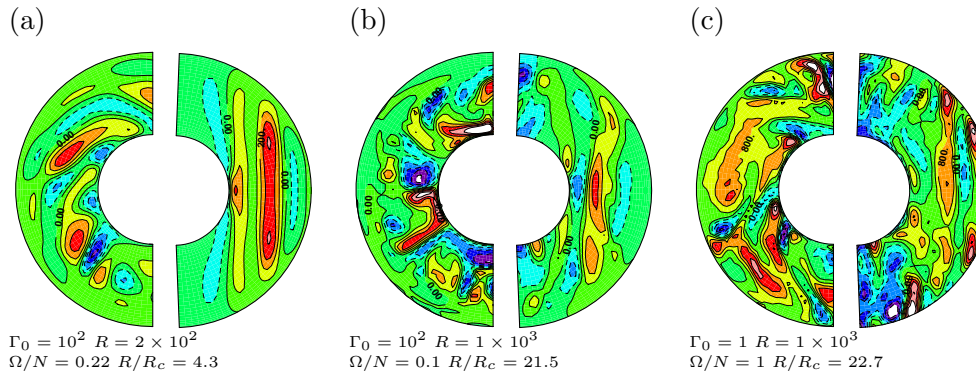|		
$\Gamma_0 = 10^2$ $R = 2 \times 10^2$	$\Gamma_0 = 10^2$ $R = 1 \times 10^3$	$\Gamma_0 = 1$ $R = 1 \times 10^3$
$\Omega/N = 0.22$ $R/R_c = 4.3$	$\Omega/N = 0.1$ $R/R_c = 21.5$	$\Omega/N = 1$ $R/R_c = 22.7$

Figure 7. Snapshots of the vorticity component in the direction of the rotating axis at the time shown in figure 5. The left-hand and right-hand panels for each case show, respectively, the equatorial cross section and the same meridional cross section as shown in figure 5. Solid lines and red regions indicate positive vorticity, and broken lines and blue regions indicate negative vorticity (colour online). The values of Γ_0 and R are the same as those of figure 5 for each case. The contour interval is 400 in (a) and (b) and 100 in (c).

columnar structure but remains confined under the stable layer. When the stratification is weakened to $\Omega/N = 1$ but the Rayleigh number is maintained approximately constant at $R/R_c = 22.7$ (figure 7(c)), the strong vorticity regions spread over the entire shell and fully erode the stable layer. Another remarkable feature is the tilting of the convection cells observed in the equatorial cross sections. The tilting of the cells is closely related to the Reynolds stress, which is one of the primary factors in the generation of mean zonal flows. In the cases of figures 7(a) and 7(c), where the equatorial mean zonal flows are prograde (figures 6(a) and 6(c)), it is clearly seen that the convection cells are tilted in the prograde outward direction. In contrast, in the case of figure 7(b), where the equatorial mean zonal flows are retrograde (figure 6(b)), tilting of the cells is not prominent in the whole shell.

When the stratification is weak, i.e., Ω/N is close to unity, both convective motions and mean zonal flows strongly penetrate the stable layer. As shown in figure 6(c), even for the case in which the Rayleigh number is 10 times greater than the critical value, the morphology of the convective motions and mean zonal flows does not change from that in the case of a smaller Rayleigh number. However, when the stratification is intense, i.e., Ω/N is smaller than unity, convective motions do not penetrate the stable layer, whereas the mean zonal flows induced by these convective motions just below the stable layer deeply penetrate the stable layer (figures 6(a) and 6(b)). Penetration of mean zonal flows in these cases is governed by viscous diffusion, because the extent of penetration is larger than the scaling by the dispersion relation of inertia-gravity waves $(\Omega/N)k_H$, and the profiles of mean zonal flows diffuse horizontally as the mean zonal flows penetrate the stratified layer in the radially outward direction. The angular momentum budget analysis performed below confirms this mechanism.

The equatorial retrograde solutions we have found are interesting because the direction of equatorial mean zonal flows changes only due to the existence of the stable layer. Again, note that these retrograde flows are not associated with the homogenization of angular momentum. The small magnitude of relative angular momentum associated with these retrograde flows compared to that of planetary angular momentum indicates that the total angular momentum is not homogenized.

In order to investigate the generation mechanism of equatorial retrograde zonal flows, we first examine whether the mean zonal flows satisfy the thermal wind balance:

$$2(\mathbf{k} \cdot \nabla)\mathbf{u} = \frac{R}{r_o}\mathbf{r} \times \nabla T. \tag{10}$$

The left-hand panels of figure 8 show the zonally averaged temperature field. In addition to positive and negative temperature deviations in the upper and lower regions, there exist latitudinal temperature differences beneath the stable layer. The right-hand panels of figure 8 are the distributions of mean zonal flows calculated with these averaged temperature fields and the equation of thermal wind balance. The mean zonal flows at the outer spherical boundary of the numerical results are used as a boundary condition when the thermal wind equation is integrated. The distributions are very similar to the numerical results in the left-hand panels of figure 6, where the temperature and mean zonal flow fields satisfy the thermal
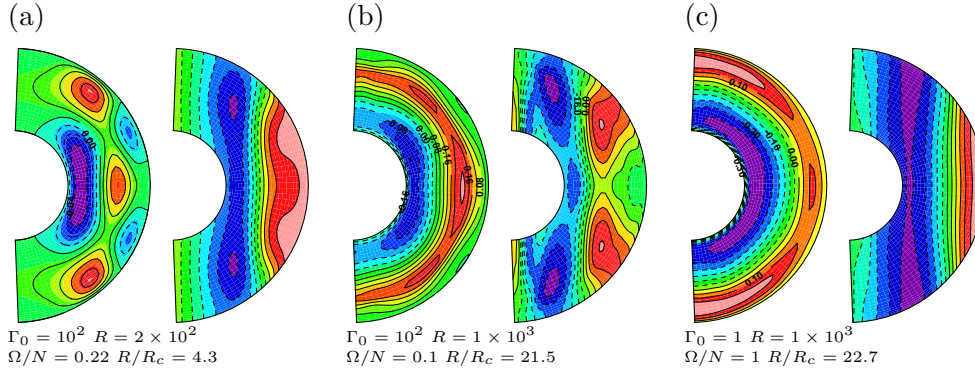
Figure 8. Zonally averaged temperature field (left) and mean zonal flows estimated by the thermal wind balance (right). The values of Γ_0 and R are the same as the values in figure 5 for each case. The contour intervals are the same as those for the left-hand panels of figure 6 (colour online).

wind balance. Note that in the case of figure 8(c), however, the mean zonal flow is not driven by the thermal wind in spite of the agreement of the zonal flow shown in figure 8(c) with the flow in figure 6(c). In this case, the right hand side of equation (10) is close to zero and the outer boundary condition mostly controls the velocity field without the deformation arising from the thermal wind relation.

Since the cause and effect relationship between the temperature and velocity fields cannot be understood from only the thermal wind balance, we perform angular momentum budget analyses. The equation of angular momentum conservation is obtained by multiplying $r \sin \theta$ by the longitudinal component of equation (2), where θ is the colatitude. The zonally averaged equation of angular momentum conservation can be expressed as follows:

$$\frac{\partial}{\partial t}(\overline{u}_\phi r \sin \theta) + \nabla \cdot \mathbf{F}_p + \nabla \cdot \mathbf{F}_r + \nabla \cdot \mathbf{F}_d + \nabla \cdot \mathbf{F}_v = 0, \tag{11}$$

where overlines denote zonally averaged quantities, u_ϕ is the longitudinal component of velocity, and

$$\mathbf{F}_p = \frac{1}{E}r^2 \sin^2 \theta(\overline{u}_\theta \mathbf{e}_\theta + \overline{u}_r \mathbf{e}_r), \tag{12}$$

$$\mathbf{F}_r = \overline{u}_\phi \overline{u}_\theta r \sin \theta \mathbf{e}_\theta + \overline{u}_\phi \overline{u}_r r \sin \theta \mathbf{e}_r, \tag{13}$$

$$\mathbf{F}_d = \overline{u'_\phi u'_\theta} r \sin \theta \mathbf{e}_\theta + \overline{u'_\phi u'_r} r \sin \theta \mathbf{e}_r, \tag{14}$$

$$\mathbf{F}_v = -r^2 \sin^2 \theta \nabla \left(\frac{\overline{u}_\phi \sin \theta}{r^2 \sin^2 \theta} \right), \tag{15}$$

where $\mathbf{F}_p$, $\mathbf{F}_r$, $\mathbf{F}_d$, and $\mathbf{F}_v$ are the planetary angular momentum flux, the relative angular momentum flux by mean meridional circulation, the angular momentum flux by the correlations of disturbances (Reynolds stresses), and the viscous angular momentum flux, respectively. Here, prime indicates the disturbance quantity defined as the deviation from the zonal average, $\mathbf{e}_\theta$, $\mathbf{e}_r$ are the unit vectors in the colatitudinal and radial directions, and u_θ is the colatitudinal component of velocity. Note that $\nabla \cdot \mathbf{F}_p = r \sin \theta[(2/E) \cos \theta \overline{u}_\theta + (2/E) \sin \theta \overline{u}_r]$ is also interpreted as the torque by Colioris force. Figure 9 shows the meridional distributions of zonally and temporally averaged angular momentum flux divergences. The distributions of $\nabla \cdot \mathbf{F}_r$ are not shown because their amplitudes are one order of magnitude smaller than the amplitudes of the other flux divergences. Note also that $\nabla \cdot \mathbf{F}_p + \nabla \cdot \mathbf{F}_r + \nabla \cdot \mathbf{F}_d = -\nabla \cdot \mathbf{F}_v$, because the values are temporally averaged and the zonal mean zonal flows are in approximately steady states.

For the case in which $\Omega/N = 0.22$ and $R/R_c = 4.30$, where the equatorial prograde zonal flow emerges, the relative angular momentum flux divergence by disturbances $\nabla \cdot \mathbf{F}_d$ dominates the planetary angular momentum flux divergence $\nabla \cdot \mathbf{F}_p$ (figure 9(a)). The distribution of $\nabla \cdot \mathbf{F}_d$ reflects the columnar convective motions that are uniform in the direction of the axis of rotation (figure 7(a)). Angular momentum is transported from the inner to outer regions of the shell through the Reynolds stress due to the tilting of the

(a)   (b)

$\Gamma_0 = 10^2 \ R = 2 \times 10^2 \ \Omega/N = 0.22 \ R/R_c = 4.3$ $\Gamma_0 = 10^2 \ R = 1 \times 10^3 \ \Omega/N = 0.1 \ R/R_c = 21.5$

(c)

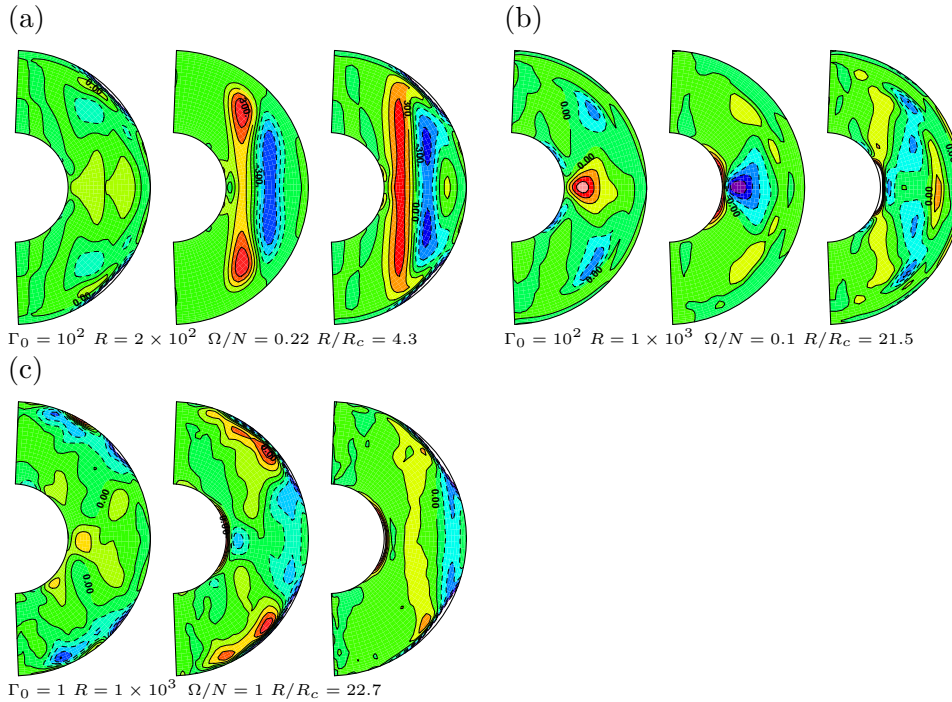$\Gamma_0 = 1 \ R = 1 \times 10^3 \ \Omega/N = 1 \ R/R_c = 22.7$

Figure 9. Distributions of zonally and temporally averaged angular momentum flux divergences. Solid lines and red regions indicate divergence, and dashed lines and blue regions denote convergence (colour online). The left-hand, center, and right-hand panels show $\nabla \cdot \mathbf{F}_p$, $\nabla \cdot \mathbf{F}_d$, and $\nabla \cdot \mathbf{F}_p + \nabla \cdot \mathbf{F}_r + \nabla \cdot \mathbf{F}_d$, respectively. The values of Γ_0 and R are the same as those in figure 5 for each case. The contour intervals are (a) 150 for all, (b) 2,000, 2,000, 800, and (c) 1,500 for all.

columnar convective vortices in the prograde outward direction, and its flux convergence in the equatorial outer region produces the equatorial prograde zonal flow below the stable layer. This configuration of angular momentum transport is the same as that in the cases without a stable layer (Takehiro and Hayashi 1999, Christensen 2002). Since the amplitudes of $\nabla \cdot \mathbf{F}_p$ and $\nabla \cdot \mathbf{F}_d$ are small in the stable layer of the equatorial region, the equatorial prograde surface flow is considered to be caused by the penetration of the zonal flow beneath the stable layer through viscous diffusion. This picture is consistent with the solution obtained by Takehiro and Lister (2002).

In addition, in the case of a larger Rayleigh number and a less strongly stratified stable layer, $\nabla \cdot \mathbf{F}_d$ produces the prograde zonal flows (figure 9(c)). Now, the convective motion perfectly penetrates the stable layer. The Reynolds stress associated with the tilting of the convective vortices seen in figure 7(c) transports angular momentum from the inner to outer regions, and produces the equatorial prograde flow. A columnar structure that is uniform in the direction of the axis of rotation cannot be observed in the distribution of $\nabla \cdot \mathbf{F}_d$ because the regular columns are deformed by the vigorous convective motions. Nevertheless, axially uniform structures can be seen in the distribution of $\nabla \cdot \mathbf{F}_p + \nabla \cdot \mathbf{F}_r + \nabla \cdot \mathbf{F}_d$ in figure 9(c).

When the stratification of the stable layer is strengthened to $\Omega/N = 0.1$, where the equatorial retrograde zonal flow emerges, $\nabla \cdot \mathbf{F}_d$ is almost in balance with $\nabla \cdot \mathbf{F}_p$ (figure 9(b)). $\mathbf{F}_d$ is convergent in the equatorial inner region, indicating the transport of angular momentum by convective disturbances from the very thin layer near the surface of the inner core. $\mathbf{F}_p$ is divergent in the equatorial region below the stratified layer and is convergent in the off-equatorial latitudes, indicating the transport of planetary angular momentum by the mean meridional circulation driven by the latitudinal thermal contrast shown in figure 8(b) (left) caused by the convective heat flux. Based on the sign of $-\nabla \cdot \mathbf{F}_v = \nabla \cdot \mathbf{F}_p + \nabla \cdot \mathbf{F}_r + \nabla \cdot \mathbf{F}_d$ the relative angular momentum flux divergence caused by disturbances $\nabla \cdot \mathbf{F}_d$ can be considered to dominate $\nabla \cdot \mathbf{F}_p$ in the equatorial inner region, whereas the planetary angular momentum flux divergence $\nabla \cdot \mathbf{F}_p$ dominates $\nabla \cdot \mathbf{F}_d$ in the equatorial outer region below the stable layer and maintains the retrograde zonal flow there. Since $\nabla \cdot \mathbf{F}_p$ and $\nabla \cdot \mathbf{F}_d$ are quite small in the stable layer, as in the case of figure 9(a), the zonal flow beneath the stable layer penetrates the surface by viscous diffusion to produce the equatorial retrograde surface flow shown in figure 9(b).

In order to confirm the validity of these arguments, figure 10 compares the amplitudes of the planetary
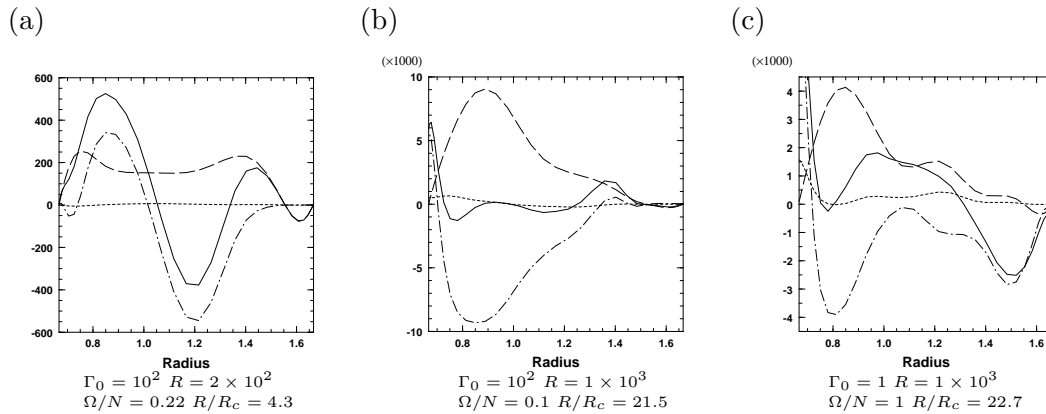
Figure 10. The radial distributions of zonally and temporally averaged angular momentum flux divergences at the equatorial cross section. Solid line denotes $\nabla \cdot \mathbf{F}_p + \nabla \cdot \mathbf{F}_r + \nabla \cdot \mathbf{F}_d$. Broken, dotted, and broken-dotted lines indicate $\nabla \cdot \mathbf{F}_p$, $\nabla \cdot \mathbf{F}_r$, and $\nabla \cdot \mathbf{F}_d$, respectively. The values of Γ_0 and R are the same as those in figure 5 for each case.

and relative angular momentum transports, $\nabla \cdot \mathbf{F}_p$, $\nabla \cdot \mathbf{F}_r$, and $\nabla \cdot \mathbf{F}_d$ at the equator. In the case of a small Rayleigh number and strong stratification, where the equatorial prograde flow emerges (figure 6(a)), $\nabla \cdot \mathbf{F}_d$ dominates in the middle and inner regions of the shell (figure 10(a)). The equatorial prograde flow is divergent in the inner region and convergent in the middle region. $\nabla \cdot \mathbf{F}_p$ dominates and is divergent just beneath the stable layer but is not strong enough for a retrograde flow to appear. In the case of the large Rayleigh number and weak stratification, where the equatorial prograde flow emerges (figure 6(c)), $\nabla \cdot \mathbf{F}_d$ governs the momentum flux convergence in the outer region of the shell (figure 10(c)). $\nabla \cdot \mathbf{F}_p$ governs the momentum flux divergence in the middle and inner regions. In the case of a large Rayleigh number and strong stratification, where the equatorial retrograde flow emerges (figure 6(b)), $\nabla \cdot \mathbf{F}_d$ slightly dominates and is convergent in the middle and inner regions, whereas $\nabla \cdot \mathbf{F}_p$ slightly dominates and is divergent in the outer region beneath the stable layer (figure 10(b)). Thus, the equatorial retrograde flow in the outer layer is induced by the planetary angular momentum flux divergence $\nabla \cdot \mathbf{F}_p$. When the Rayleigh number is further increased, $\nabla \cdot \mathbf{F}_d$ changes to positive in the outer region and enhances retrograde zonal flow generation (not shown). The retrograde zonal flow induced by $\nabla \cdot \mathbf{F}_p$ is considered to tilt the convective vortices in the retrograde outward direction. Note that the magnitudes of $\nabla \cdot \mathbf{F}_p$ and $\nabla \cdot \mathbf{F}_d$ are quite small in the stable layer. This means that the mean zonal flow in the stable layer is passively generated through viscous diffusion.

4   DISCUSSION

We performed numerical experiments of finite amplitude thermal convection in a rotating spherical shell accompanied by an upper stably stratified layer. The results reveal that equatorial prograde mean zonal flows at the top boundary are induced when the Rayleigh number is as small as several times larger than the critical value, whereas when the Rayleigh number is increased to approximately several dozen times larger than the critical value, equatorial retrograde flows are generated for the cases with strong stratification of the stable layer. The existence of a strongly stratified outer layer appears to promote retrograde equatorial zonal flows.

These retrograde flows are not associated with the homogenization of angular momentum. The results of the angular momentum budget analysis indicate that the planetary angular momentum transport by mean meridional circulation primarily contributes to the generation of the equatorial retrograde zonal flow emerging in the case with a strong stratified outer layer. The contribution of the angular momentum transport by the Reynolds stress, which dominates the total transport in the case with a weakly stratified layer, becomes relatively small. The latitudinal temperature gradient produced below the stable layer by the convective heat transport induces a mean meridional circulation, which removes the planetary angular momentum and generates the equatorial retrograde flow there. The retrograde flow beneath the stable layer diffuses towards the surface by viscosity.
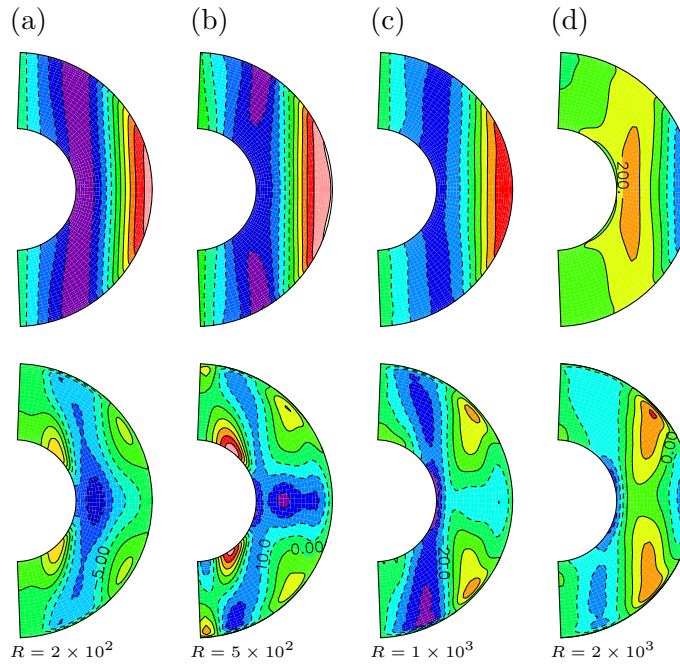
(a)   (b)   (c)   (d)

$R = 2 \times 10^2$ $R = 5 \times 10^2$ $R = 1 \times 10^3$ $R = 2 \times 10^3$

Figure 11.   Distributions of mean zonal flows when rigid boundaries are given just below the stable layer. $r_i = 0.6667, r_o = 1.5$, and $r_b = 10.5$. The upper and lower panels show the cases of free-slip and no-slip conditions at the top boundary, respectively. Solid lines and red regions indicate the prograde direction, and broken lines and blue regions indicate the retrograde direction (colour online). (a) $R = 2 \times 10^2$; the contour intervals are 5 and 2.5 for the upper and lower panels, respectively. (b) $R = 5 \times 10^2$; the contour intervals are 20 and 5 for the upper and lower panels, respectively. (c) $R = 1 \times 10^3$; the contour intervals are 40 and 10 for the upper and lower panels, respectively. (d) $R = 2 \times 10^3$; the contour intervals are 100 and 20 for the upper and lower panels, respectively.

The reason that the contribution of the Reynolds stress becomes small and the planetary angular momentum transport dominates might be explained by the change in the effective dynamic boundary condition at the bottom of the stable layer. The bottom boundary of the stable layer is expected to behave as an impermeable boundary when the stratification is strengthened. In order to confirm this expectation, we perform additional numerical experiments: We place a rigid boundary at the base of the stable layer and remove the stable layer. We adopted two types of dynamic boundary conditions, namely, the free-slip and no-slip conditions, as extreme cases. Figure 11 shows the obtained mean zonal flows. In the case of the free-slip dynamic boundary condition, the equatorial zonal flows tend to be prograde and become retrograde only when the Rayleigh number is increased to 2×10^3. On the other hand, when the boundary condition is no-slip, the equatorial zonal flow is already retrograde at the Rayleigh number of 2×10^2.

Compared to the results shown in figure 2, the distribution of zonal flow obtained with the free-slip boundary more closely resembles that of figure 2(a) when the Rayleigh number is 2×10^2. However, when the Rayleigh number is larger than or equal to 5×10^2, the distributions obtained with a no-slip boundary more closely resemble those shown in figures 2(b) through 2(d). The existence of the stable layer causes the bottom of the stable layer to behaves as a virtual boundary for the convective motion underneath. Its effective dynamic condition appears to vary from the free-slip condition to the no-slip condition as the Rayleigh number increases. Interestingly, the introduction of a strongly stratified layer corresponds to a no-slip virtual boundary rather than a free-slip boundary. The latter boundary might be the condition that we intuitively imagine to hold. The viscous effect, which is often neglected in atmospheric problems, plays a crucial role in the present problem. A strongly stable layer inhibits penetration of turbulent fluid motion underneath. As a result, velocity vanishs within the stable layer. Viscosity should operate on this radial shear flow. Consequently, the result appears to be similar to the case with a no-slip boundary.

In order to confirm whether the dynamic condition beneath the stable layer is close to the no-slip condition in the high-Rayleigh-number cases, figure 12 shows the distributions of time averaged tangential viscous stress in meridional cross sections. For the case of the outer stably stratified layer (figure 12(a)), strong tangential stress regions concentrate around the bottom of the stable layer. In the no-slip case (figure 12(c)), strong tangential stress layers stick to the outer no-slip boundary. On the other hand, in the free-slip case (figure 12(b)), prominent strong tangential stress regions cannot be seen. Figure 12 suggests
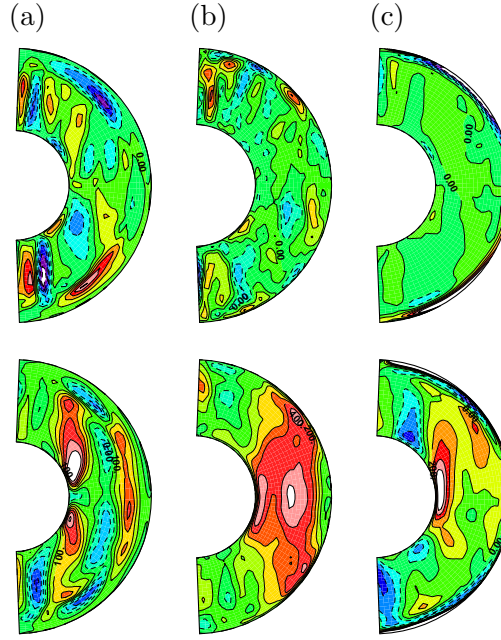
(a)　　　　　　(b)　　　　　　(c)

Figure 12. Distributions of time averaged tangential viscous stress in meridional cross sections for $R = 1 \times 10^3$. The upper and lower panels show the latitude–radial, and radial–longitude components, respectively (colour online). (a) Case with a stably stratified layer with $\Gamma = 10^2$ and $r_b = 1.5$. The contour intervals are 40 and 50, respectively. (b) Case with a stress-free outer boundary with $r_o = 1.5$. The contour intervals are 50 and 100, respectively. (c) Case with a no-slip outer boundary with $r_o = 1.5$. The contour intervals are 1,000 and 100, respectively

(a) $R = 2 \times 10^2$　　(b) $R = 5 \times 10^2$　　(c) $R = 1 \times 10^3$　　(d) $R = 2 \times 10^3$
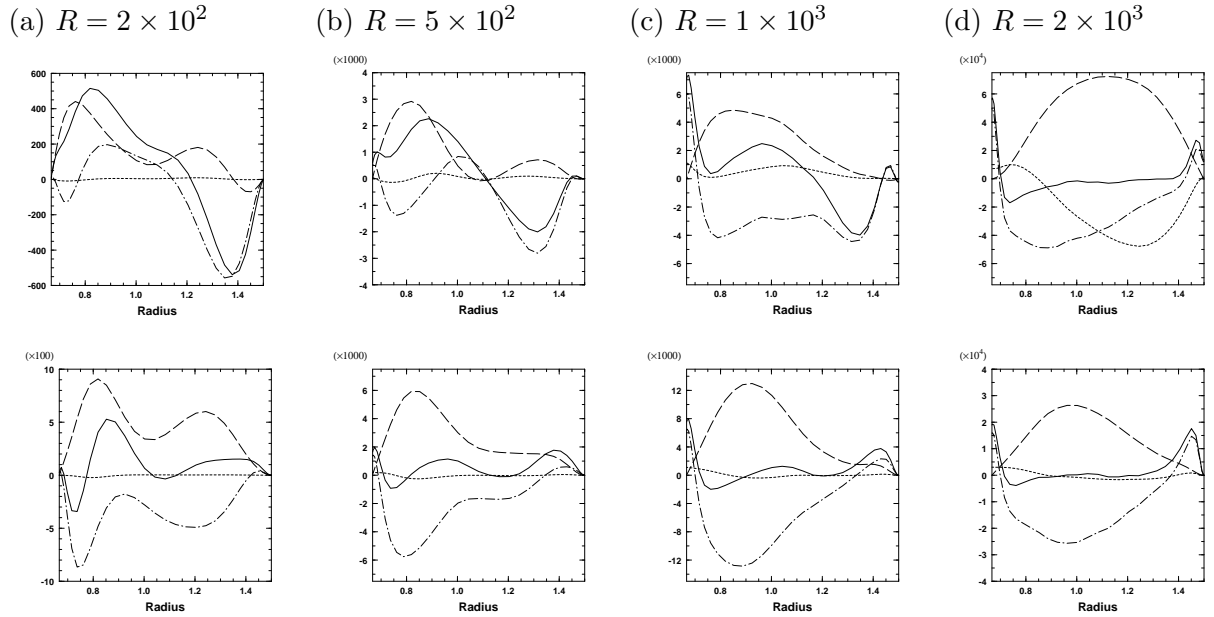

Figure 13. Distributions of zonally and temporally averaged angular momentum flux divergences for the cases of figure 11. The solid line denotes $\nabla \cdot \mathbf{F}_p + \nabla \cdot \mathbf{F}_r + \nabla \cdot \mathbf{F}_d$. The broken, dotted, and broken-dotted lines indicate $\nabla \cdot \mathbf{F}_p$, $\nabla \cdot \mathbf{F}_r$, and $\nabla \cdot \mathbf{F}_d$, respectively. The upper and lower panels indicate the cases of the free-slip and no-slip conditions at the top boundary, respectively. (a) $R = 2 \times 10^2$, (b) $R = 5 \times 10^2$, (c) $R = 1 \times 10^3$, (d) $R = 2 \times 10^3$.

that the tangential stress distribution of the stably stratified layer case is similar to that of the no-slip boundary case rather than the free-slip case.

Figure 13 examines the effective dynamic condition just below the stably stratified layer from the viewpoint of the angular momentum budget. In the cases of the free-slip condition on the outer boundary (upper panels of figure 13), the relative angular momentum flux divergence by disturbances $\nabla \cdot \mathbf{F}_d$ dominates and produces equatorial surface prograde flows when the Rayleigh numbers are not so large ($R \leq 1 \times 10^3$).

When the Rayleigh number is increased to $R = 2 \times 10^3$, the contribution of the relative angular momentum flux caused by mean meridional circulation $\nabla \cdot \mathbf{F}_r$ becomes large and cancels the planetary angular momentum flux caused by mean meridional circulation $\nabla \cdot \mathbf{F}_p$, suggesting the occurrence of angular momentum homogenization, which produces an equatorial surface retrograde flow. The appearance of positive $\nabla \cdot \mathbf{F}_d$ near the surface is due to tilting of disturbances by the zonal shear flow. On the other hand, in the cases of the no-slip condition on the outer boundary (lower panels of figure 13), $\nabla \cdot \mathbf{F}_p$ slightly dominates $\nabla \cdot \mathbf{F}_d$ and produces equatorial retrograde flows when the Rayleigh number is small as $R = 2 \sim 5 \times 10^2$. When the Rayleigh number is increased to $R = 1 \sim 2 \times 10^3$, the contribution of $\nabla \cdot \mathbf{F}_d$ becomes large in the equatorial surface layer, which again results from tilting of disturbances caused by the zonal shear flow. Comparing figures 13 and 10 for the stable layer experiments, the morphology of the angular momentum budget in the case of a small Rayleigh number (figure 10(a)) is similar to that for the case with the free-slip condition (upper panel of figure 13(a)), whereas the morphology of the angular momentum budget in the case of a large Rayleigh number (figure 10(b)) is similar to those for the cases of the no-slip condition (lower panels of figure 13(b) and 13(c)). This indicates that the angular momentum budget analysis also supports the hypothesis that the effective dynamic condition just below the stratified layer varies from the free-slip condition to the no-slip condition as the Rayleigh number increases.

Gilman (1977) and Aurnou *et al.* (2007) show that transition of equatorial mean zonal flow from prograde to retrograde occurs when the Rayleigh number is increased. They considered standard experimental setups involving thermal convection in a rotating spherical shell without a stably stratified layer. They reported that mixing of angular momentum by vigorous turbulent convection results in retrograde equatorial surface flows when the Rayleigh number becomes so large that the inertial force dominates the Coriolis force and argued that the transition occurs when $R^* \equiv \alpha g_0 \Delta T / (\Omega^2 D)$ is equal to a critical value R_c^*, which is on the order of unity. Since, in our formulation, $R^* = RE$, the transition in the experiments of the present study, which occurs at around $R \sim O(10^3)$ (figure 4), indicates that $R_c^* \sim O(10^3) \times 10^{-3} = O(1)$. Although the present results with a stably stratified layer might appear to be consistent with their discussion, this argument is not sufficiently precise.

Detailed observation of the results of our additional numerical experiments indicate that R_c^* depends on the dynamic boundary condition. As shown in the upper panels of figures 11(c) and 11(d), we find that R_c^* is approximately 0.9 under the free-slip upper boundary condition. On the other hand, as shown in the lower panel of figure 11(a), R_c^* is smaller than approximately 0.1(!) under the no-slip upper boundary condition [1]. The results shown in figure 2 are consistent with this dependency of R_c^* on the upper dynamic boundary condition. When the Rayleigh number is increased, the effective dynamic boundary condition just below the stable layer changes from the free-slip to no-slip condition, resulting a decrease in R_c^*. Then, R^* becomes larger than R_c^*, and the transition to the equatorial retrograde regime occurs between figures 2(a) and 2(b), where $R^* = 0.12$ and 0.28, respectively.

The fact that R_c^* is smaller than the order of unity under the top no-slip boundary condition is consistent with the fact that the retrograde equatorial zonal flows are not caused by the vigorous mixing of angular momentum. Figure 13 presents the latitudinal distributions of total angular momentum at the outer surface for the mean zonal flows shown in figure 11. The retrograde flows at $R = 2 \times 10^3$ in the case of the free-slip boundary condition is caused by the mixing of angular momentum. On the other hand, in the cases of the no-slip boundary condition, the mixing of angular momentum is relatively ineffective. The amplitude of the mean zonal velocity is small, and the total angular momentum is approximately equal to the planetary angular momentum (not shown).

The equatorial prograde acceleration, usually produced by the Reynolds stress caused by the tilting of the columnar convective motion, appears to be ineffective for the upper no-slip condition. This might be a result of the possible decrease in the radial extent of the convective spiral structure when the no-slip boundary condition is applied. Takehiro (2008) discussed the use of a two-dimensional rapidly rotating annulus model in which the radial extent of spiral convection emerging in a rotating spherical shell is related to the radial propagation distance of the topographic Rossby waves emitted from the inner to outer regions.

---

[1] Note that the dynamic boundary conditions of our experiments are different from those of Aurnou *et al.* (2007). We adopt the top no-slip or free-slip condition and the bottom free-slip condition, whereas they adopted the top free-slip condition and the bottom free-slip or no-slip condition.
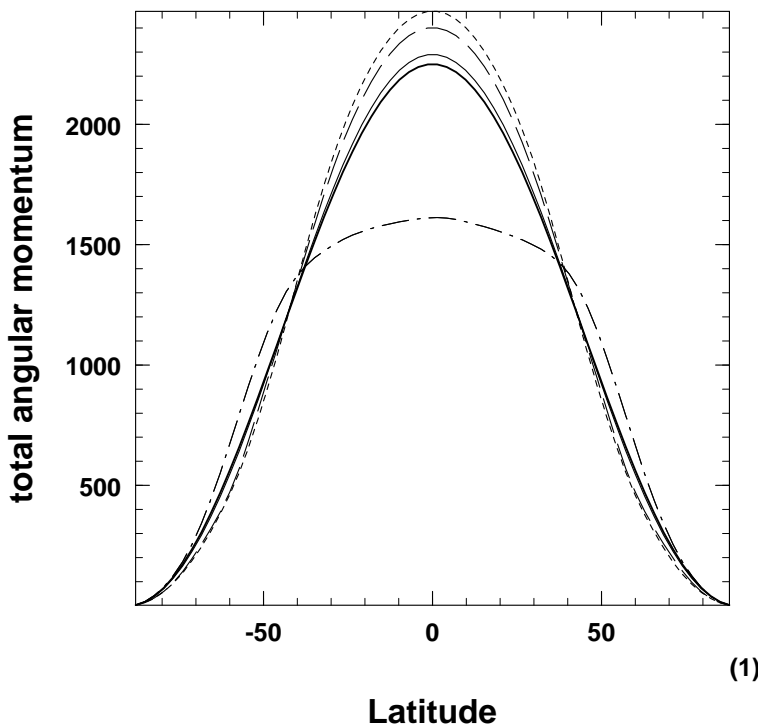
Figure 14.   Latitudinal profiles of the total angular momentum at the outer boundary ($r = 1.5$) for the mean zonal flows shown in Figure 11. Thin solid, dashed, dotted, and dash-dotted lines indicate the cases of $R = 2 \times 10^2$, 5×10^2, 1×10^3, and 2×10^3, respectively, with the free-slip condition at the top boundary. Thick solid lines indicate the cases with the no-slip condition at the top boundary, i.e., total angular momentum of the rigid rotating state.

From the viewpoint of Rossby wave propagation, the no-slip boundary condition is expected to decrease the amplitudes of Rossby waves faster as they propagate and to decrease the radial extent of the spiral structure. However, there have been few studies comparing thermal convections and induced mean zonal flows between under the no-slip and free-slip conditions. Zhang *et al.* (2007) obtained asymptotic solutions of thermal convection in a rapidly rotating sphere under the no-slip boundary condition. Although the mathematical expressions of their solutions plausibly include the difference in convective structure between the dynamic boundary conditions, no solutions were reported because their primary goal was to reveal the Prandtl number dependence. It is necessary to compare the structure of convection, its Reynolds stress, and the induced zonal flow under different dynamic boundary conditions.

We have performed a series of numerical experiments for fixed values of the thickness of the stable layer and the rotating speed of the spherical shell. The behavior of the solutions of the equatorial retrograde flows obtained in the present study has not yet been well examined for the other values of these parameters. However, when the thickness of the stable layer is decreased, it is expected that the equatorial retrograde zonal flow disappears because the effect of the outer boundary becomes prominent. Preliminary numerical experiments have demonstrated that the equatorial retrograde solution switches to the prograde solution at around $r_b = 1.65$. Conversely, when the depth of the stable layer is increased, the equatorial retrograde flow still emerges even at $r_b = 1.2$. Thus far, cases involving higher rotational speeds could not be investigated because of limited computing resources. However, a numerical simulation of the MHD dynamo in a rotating spherical shell with an outer stably stratified layer is interesting as an example of a lower-Ekman-number case. Christensen (2006) obtained the retrograde flow in the equatorial outer region when the Ekman number is as small as $O(10^{-5})$. On the other hand, in experiments on a thinner stable layer performed by Stanley and Mohammadi (2008), an equatorial prograde surface flow emerged. Christensen and Wicht (2008) presented a series of numerical MHD dynamo experiments with a deep, stable layer, one of which revealed an equatorial prograde surface flow. It is important to investigate the differences in the generation mechanisms of these prograde/retrograde equatorial flows by extending the results of the present study.

We have demonstrated that, for strong stratification, the stable layer imposes a rigid, rather than stress-

free, condition on the underlying flow. This rigid condition prevents the Reynolds-stress mechanism from acting efficiently, and, therefore, the thermal wind effect seems to dominate instead. However, we should refrain from applying these results to actual planetary atmospheres. First, we explore a rather larger Ekman number of $E = 10^{-3}$, which may limit their applicability. Viscous effects, which play an important role in the investigated mechanisms, might be too large compared to actual situations. When the Ekman number becomes smaller, the present mechanism of retrograde zonal flow generation might not function. Second, the outer stable layers in the planetary atmospheres would be much thinner than in the proposed model. It might be difficult to confirm that the outermost, rather thin, stable layers would have an impact on the dynamics of the much thicker, deep regions. In addition, the effects of compressibility and radiation transfer should be taken into account in applications involving real atmospheres.

REFERENCES

Aurnou J.M. and Olson, P.L., Strong zonal winds from thermal convection in a rotating spherical shell, *Geophys. Res. Lett.* 2001, **28**, 2557–2559.

Aurnou, J., Heimpel M. and Wicht, J., The effects of vigorous mixing in a convective model of zonal flow on the ice giants, *Icarus* 2007, **190**, 110–126.

Aurnou, J., Heimpel, M., Allen, L., King E. and Wicht, J., Convective heat transfer and pattern of thermal emission on the gas giants, *Geophys. J. Int.* 2008, **173**, 793–801.

Busse, F. H., Differential rotation in stellar convection zones. *Astrophys. J.* 1970, **159**, 629–639.

Christensen, U. R., Zonal flow driven by strongly supercritical convection in rotating spherical shells, *J. Fluid Mech.* 2002, **470**, 115–133.

Christensen, U.R., A deep dynamo generating Mercury's magnetic field, *Nature* 2006, **444**, 1056–1058.

Christensen, U.R. and Wicht, J., Models of magnetic field generation in partly stable planetary cores: Applications to Mercury and Saturn. *Icarus* 2008, **196**, 16–34.

Garcia-Melendo, E. and Sanchez-Lavega, A., A study of the stability of Jovian zonal winds form HST Images: 1995-2000, *Icarus* 2001, **152**, 316–330.

Gilman, P.A., Nonlinear dynamics of Boussinesq convection in a deep rotating spherical shell –I, *Geophys. Astrophys. Fluid Dyn.* 1977, **8**, 93–135.

Glatzmaier, G.A., Martha E. and Tamara, M.R., Differential rotation in giant planets maintained by density-stratified turbulent convection, *Geophys. Astrophys. Fluid Dyn.* 2009, **103**, 31–51.

Guillot, T., Interior of giant planets inside and outside the solar system, *Science* 1999, **286**, 72–77.

Guillot, T., The interiors of giant planets: models and outstanding questions, *Ann. Rev. Earth Planet. Sci.* 2005, **33**, 493–530.

Hammel, H.B., de Pater, I., Gibbard, S., Lockwood, G.W. and Rages, K., Uranus in 2003: Zonal winds, banded structures, and discrete features, *Icarus* 2005, **175**, 534–545.

Heimpel M. and Aurnou, J., Turbulent convection in rapidly rotating spherical shells: A model for equatorial and high latitude jets on Jupiter and Saturn, *Icarus* 2007, **187**, 540–557.

Hunt, G.E., The atmospheres of the outer planets, *Ann. Rev. Earth Planet. Sci.* 1983, **11**, 415–459.

Pearl J.C. and Conrath, B.J., The albedo, effective temperature, and energy balance of Neptune, as determined from Voyager data, *J. Gephys. Res.* 1991, **96**, 18921–18930.

Sanchez-Lavega, A., Rojas, J. and Sada, P., Saturn's zonal wind at cloud level, *Icarus* 2000, **147**, 405–420.

Schubert, G., Chan, K. H., Liao, X. and Zhang, K., Planetary dynamos: effects of electrically conducting flows overlying turbulent regions of magnetic field generation. *Icarus*, 2004, **172**, 305–315.

Seiff, A., Kirk, D.B., Knight, T.C.D., Mihalov, J D., Blanchard, R.C., Young, R.E., Schubert, G., Zhang, U., Lehmacher, G., Milos, F.S. and Wang, J., Structure of the atmospheric of Jupiter: Galileo probe measurements, *Science* 1996, **272**, 844–845.

Sromovsky, L.A., Fry, P.M., Dowling, T.E., Baines, K.H. and Limaye, S.S., Coordinated 1996 HST and IRTF imaging of Neptune and Triton: III. Neptune's atmospheric circulation and cloud structure, *Icarus* 2001, **149**, 459–488.

Stanley S. and Mohammadi, A., Effects of an outer thin stably stratied layer on planetary dynamos" *Phys. Earth Planet. Inter.* 2008, **168**, 179–190.

Sugiyama, K., Odaka, M., Kuramoto, K. and Hayashi, Y.-Y., Static stability of the Jovian atmospheres estimated from moist adiabatic profiles, *Geophys. Res. Lett.* 2006, **33** L03201, doi:10.1029/2005GL024554

Takehiro S. and Hayashi, Y.-Y., Mean zonal flows excited by critical thermal convection in rotating spherical shells, *Geophys. Astrophys. Fluid Dyn.* 1999, **90**, 43–77.

Takehiro S. and Lister, J.R., Penetration of columnar convection in an outer stably stratified layer in rapidly rotating spherical fluid shells, *Earth Planet. Sci. Lett.* 2001, **187**, 357–366.

Takehiro S. and Lister, J.R., Surface zonal flows induced by thermal convection trapped below a stably stratified layer in a rapidly rotating spherical shell," *Geophy. Res. Lett.* 2002, **29**, 10.1029/2002GL015450

Takehiro, S., Odaka, M., Ishioka, K., Ishiwatari, M., Hayashi Y.-Y. and SPMODEL Development Group, A series of hierarchical spectral models for geophysical fluid dynamics, *Nagare Multimedia* 2006, Available online at: http://www.nagare.or.jp/mm/2006/spmodel/

Takehiro, S., Physical interpretation of spiralling-columnar convection in a rapidly rotating annulus with radial propagation properties of Rossby waves, *J. Fluid Mech.* 2008, **614**, 67–86.

Thompson, M.J., Toomre, J., Anderson, E.R., Antia, H.M., Berthomieu, G., Burtonclay, D., Chitre, S.M., Christensen-Dalsgaard, J., Corbard, T., DeRosa, M., Genovese, C.R., Gough, D.O., Haber, D.A., Harvey, J.W., Hill, F., Howe, R., Korzennik, S.G., Kosovichev, A.G., Leibacher, J.W., Pijpers, F.P., Provost, J., Rhodes Jr., J., Schou, J., Sekii, T., Stark, P.B. and Wilson, P.R., Differential rotation and dynamics of the solar interior, *Science* 1996, **272**, 1300–1305.

Zhang, K., Spiralling columnar convection in rapidly rotating spherical fluid shells, *J. Fluid Mech.* 1992 **236**, 535–556.

Zhang, K. and Schubert, G., Penetrative convection and zonal flow on Jupiter, *Science* 1996, **273**, 941–943.

Zhang, K. and Schubert, G., Linear penetrative spherical rotating convection, *J. Atmos. Sci.* 1997, **54**, 2509–2518.

Zhang, K., Liao, X. and Busse, F.H., Asymptotic solutions of convection in rapidly rotating non-slip spheres, *J. Fluid Mech.* 2007, **587**, 371–380.